Expansion of a collisionless hypersonic plasma plume into a vacuum

Yuan Hu and Joseph Wang*
Department of Astronautical Engineering, University of Southern California, Los Angeles, California 90089-1192, USA

(Received 24 April 2018; published 20 August 2018)

Both fully kinetic and hybrid particle-in-cell (PIC) simulations are performed to investigate the two-dimensional (2D) expansion of a collisionless, hypersonic plasma plume into a vacuum. The fully kinetic PIC simulations are carried out using the real ion-to-electron mass ratios of H^+, Ar^+, and Xe^+, while the hybrid PIC model assumes the electrons to be a massless, isothermal fluid. We find that the hypersonic plasma plume exhibits four distinct regions, the unperturbed, quasisteady expansion, self-similar expansion and electron front regions. The behavior of electrons is strongly anisotropic, causing considerably different expansion characteristics between the plume direction and the transverse direction. Along the plume direction, the expansion dynamics is similar to that of the classical one-dimensional (1D) semi-infinite plasma expansion and the electrons are almost isothermal. In the transverse direction, the expansion process can be considered analogous to the 1D expansion of a finite plasma where the effect of electron cooling is important. This anisotropic characteristic is attributed to the amount of electron thermal energy available from the source in different directions. A direct comparison between the hybrid and full PIC simulations shows that the widely used equilibrium isothermal electron fluid model is in general not valid for modeling the expansion of a collisionless plasma plume.

DOI: 10.1103/PhysRevE.98.023204

I. INTRODUCTION

This paper considers the expansion of a collisionless plasma plume into a vacuum. The plasma plume at the emission source is quasineutral and has a plume velocity v_0 for both the ions and electrons. The ions are cold and hypersonic with a thermal velocity $v_{ti0} \ll v_0$ and a Mach number $M_0 = v_0/C_{s0} \gg 1$, where C_{s0} is the ion acoustic velocity. The electrons are thermal with a thermal velocity $v_{te0} > v_0$. The associated expansion process not only is a fundamental problem in plasma dynamics but also appears in many plasma engineering applications. An important example is the plasma plume emitted by an electric propulsion (EP) thruster. An EP thruster emits a low density plasma plume of cold beam ions and thermal electrons with a flow characteristic of $v_{ti0} < C_{s0} \ll v_0 < v_{te0}$ [1,2]. The plume becomes quasineutral almost immediately downstream of the thruster exit. The collision mean free path is also much larger than the flow characteristic length of the plume. The expansion process not only determines the plume structure but also plays an important role in EP plume-spacecraft interactions [2–4].

As a classical topic in plasma physics, plasma expansion has been studied extensively using one-dimensional (1D) models. According to the initial size of plasma, one may distinguish between the semi-infinite plasma [5–12] and the finite plasma [13–21] in a 1D plasma expansion. These 1D studies showed that there are significant differences between the semi-infinite plasma expansion and the finite plasma expansion. For instance, the self-similar solution to a semi-inifinite plasma expansion in x showed that the potential Φ drop is proportional to x [5,6], while that to a finite plasma expansion predicted a quadratic dependence of potential decrease along x [14]. Moreover, in a semi-infinite plasma expansion, the ion front velocity exhibits a logarithmic dependence on time and the final ion velocity is indefinite [8,10]. In contrast, in a finite-size plasma expansion, the ion acceleration is limited [16,17,19,20].

The expansion of a plasma plume into a vacuum happens in two (2D) or three (3D) dimensions, and is qualitatively different from the 1D process. The studies of plasma expansion in dimensions higher than 1D mostly rely on numerical simulations. The particle-in-cell (PIC) method [22] is a conventional tool for kinetic simulations of the collisionless plasma expansion. According to how the electrons are handled in a numerical model, one can distinguish between hybrid PIC models, in which the ions are treated as particles while the electrons are considered to be a fluid, and fully kinetic or full particle PIC models, in which both the electrons and ions are treated as particles. To save on computational time, many studies of 2D or 3D plume expansion adopt the fluid approximation for electrons and apply the hybrid PIC approach. The electron fluid models used in the past hybrid PIC simulations may be categorized as isothermal fluid models [2,23–26], or local temperature-dependent models [27–31]. In particular, the isothermal electron model plus the assumption of massless electrons yields the Boltzmann relation,

$$n_e = n_0 \exp\left[\frac{e(\Phi - \Phi_0)}{k_b T_{e0}}\right], \tag{1}$$

where "0" in the subscript indicates the parameters at the reference point, and n_e, Φ, T_e, k_b, and e denote the electron density, electric potential, electron temperature, Boltzmann constant, and elementary charge, respectively. Equation (1) is the most widely used assumption for modeling electrons in hybrid PIC simulations.

*josephjw@usc.edu

Regardless of the specific models used for electrons, the fluid treatment of electrons is valid only when the electrons are in an equilibrium or near-equilibrium state. This requires frequent collisions between particles, a condition not satisfied in a collisionless plasma plume. Recently, analytical models taking into account the electron kinetics were applied to study the 1D finite-size plasma expansion [20,21,32] and the plasma expansion in a magnetic nozzle [33–36]. For 2D or 3D expansion problems, fully kinetic PIC simulations were carried out to study the EP plasma plume [3,37–42] as well as the laser-irradiated plasma plume [43–45]. In particular, Hu and Wang [41,42] studied the influence of electrons' microscopic kinetic characteristics in a EP plasma plume and found that the electrons are mostly nonequilibrium and the electron temperature is highly anisotropic.

However, to address the validity or the effects of using a fluid treatment of electrons in the expansion of a finite-size collisionless plasma plume, a direct comparison between the hybrid and full PIC simulations is needed. Few studies have carried out such direct comparisons because fully kinetic PIC simulations of multidimensional plume expansion are very computationally demanding. Fully kinetic PIC simulations are carried out at the electron timescale, but the simulations need to run for at least several tens of ion plasma periods so that the plume expansion region can fully develop. A large simulation domain is also necessary to minimize the effects of domain boundary conditions. Moreover, to preserve the correct velocity order for ions and electrons ($v_{ti0} < C_{s0} \ll v_0 < v_{te0}$) in the plume, using an artificially reduced ion-to-electron mass ratio is often not valid for such simulations. Using the correct ion-to-electron mass ratio in a simulation is also desired for application studies related to EP, which uses Xe^+ as the propellant species in flight and Ar^+ in ground testing. Very recently, Pfeiffer *et al.* [46] made one of the first such attempts for an Al^+ plume expansion. However, their direct comparison between the hybrid and full PIC simulation results is meaningful only within a very short timescale due to the small simulation domain used.

This paper carries out both hybrid PIC and large-scale fully kinetic PIC simulations of a collisionless plasma plume expansion and presents a direct comparison between the two approaches. Results are presented on 2D plume dynamics, and the electron and ion characteristics in the expansion. A quantitative assessment of the effects of an electron fluid model on the collisionless hypersonic plasma plume expansion is also discussed. As Ar^+ and Xe^+ are the two commonly used propellent species in EP, the effects of ion-to-electron mass ratio on the expansion are also examined by considering H^+, Ar^+, and Xe^+ in the full PIC simulations.

II. NUMERICAL METHOD AND SIMULATION SETUP

In this section, the governing equations are given in the normalized and dimensionless form, indicated by the notation "˜". In PIC simulations, the dynamics of a particle is governed by the Newton's law of motion,

$$\tilde{\mathbf{v}} = \frac{d\tilde{\mathbf{x}}}{d\tilde{t}}, \quad \frac{d}{d\tilde{t}}(\tilde{m}\tilde{\mathbf{v}}) = \tilde{\mathbf{F}}. \tag{2}$$

In Eq. (2), $\tilde{\mathbf{x}} = (\tilde{x}, \tilde{y}, \tilde{z})$, $\tilde{\mathbf{v}} = (\tilde{v}_x, \tilde{v}_y, \tilde{v}_z)$, and $\tilde{m}$ are the instantaneous position vector, velocity vector, and mass of a particle, respectively, $\tilde{t}$ is the time, and $\tilde{\mathbf{F}}$ is the force exerted on a particle. Only the electrostatic force is taken into account in this paper,

$$\tilde{\mathbf{F}} = \tilde{q}\,\tilde{\mathbf{E}}, \quad \tilde{\mathbf{E}} = -\tilde{\nabla}\tilde{\Phi}, \tag{3}$$

where $\tilde{q}$ is the charge, $\tilde{\mathbf{E}}$ is the electric field vector, and $\tilde{\Phi}$ is the electric potential obtained by self-consistently solving the Poisson's equation, Eq. (4),

$$-\tilde{\nabla}^2\tilde{\Phi} = (Z\tilde{n}_i - \tilde{n}_e), \tag{4}$$

where Z is the ion charge number, and $\tilde{n}_i$ and $\tilde{n}_e$ are the ion and electron number densities, respectively. In Eq. (4), both $\tilde{n}_i$ and $\tilde{n}_e$ are obtained from gathering the number of macroparticles deposited to the mesh points for the full PIC simulations. For the hybrid PIC simulations, $\tilde{n}_i$ is still obtained from the particle information, but $\tilde{n}_e$ is the result from solving the equations of fluid dynamics. Depending on the assumptions made to the electron fluid, the difficulty in getting $\tilde{n}_e$ differs. In this study, we adopt the most commonly used Boltzmann electron fluid model given by Eq. (1) for the hybrid simulation.

The reference physical quantities used for normalization must be carefully selected to reflect the spatial and timescales that a modeling attempts to capture. The fully kinetic PIC resolves the physics at the electron scale while the hybrid PIC only simulates the ion kinetic scale processes. Hence, the fully kinetic PIC uses dimensionless variables normalized by the electron plasma parameters, and the hybrid PIC uses those normalized by the ion plasma parameters. The normalization used for the fully kinetic PIC is as follows:

$$\tilde{m} = \frac{m}{m_e}, \quad \tilde{t} = t\omega_{pe0}, \quad \tilde{\mathbf{v}} = \frac{\mathbf{v}}{v_{te0}}, \quad \tilde{\mathbf{x}} = \frac{\mathbf{x}}{\lambda_{D0}},$$
$$\tilde{n} = \frac{n}{n_0}, \quad \tilde{q} = \frac{q}{e}, \quad \tilde{\Phi} = \frac{e\Phi}{k_b T_{e0}}, \tag{5}$$

and that for the hybrid PIC is,

$$\tilde{m} = \frac{m}{m_i}, \quad \tilde{t} = t\omega_{pi0}, \quad \tilde{\mathbf{v}} = \frac{\mathbf{v}}{C_{s0}}, \quad \tilde{\mathbf{x}} = \frac{\mathbf{x}}{\lambda_{D0}},$$
$$\tilde{n} = \frac{n}{n_0}, \quad \tilde{q} = \frac{q}{e}, \quad \tilde{\Phi} = \frac{e\Phi}{k_b T_{e0}}. \tag{6}$$

In Eqs. (5) and (6), the subscript "0" denotes the parameters at the plume exit surface, which is used as the reference condition. $\lambda_{D0} = \sqrt{\epsilon_0 k_b T_{e0}/n_0 e^2}$ is the Debye length. m_e and $\omega_{pe0} = \sqrt{n_0 e^2/\epsilon_0 m_e}$ are the mass and plasma frequency of electron, respectively. m_i and $\omega_{pi0} = \sqrt{n_0 e^2/\epsilon_0 m_i}$ are the mass and plasma frequency of ion, respectively. $v_{te0} = \sqrt{k_b T_{e0}/m_e}$ is the electron thermal velocity. $C_{s0} = \sqrt{k_b T_{e0}/m_i}$ is the ion acoustic velocity. e denotes the elementary charge, ϵ_0 is the vacuum permittivity and k_b is the Boltzmann constant. It is noted that the normalization for the fully kinetic [Eq. (5)] and that for the hybrid PIC modeling [Eq. (6)] differ in the mass ($\tilde{m}$), time ($\tilde{t}$) and velocity ($\tilde{\mathbf{v}}$). As $\omega_{pi0} \ll \omega_{pe0}$, the hybrid PIC simulation is performed with a much larger time step than that for the full particle PIC, thereby accelerating the simulation.

Figure 1 illustrates the simulation setup in this study. The simulation domain is a rectangular box with $L_x \times L_y = 2000\lambda_{D0} \times 1000\lambda_{D0}$. The emission source is positioned in

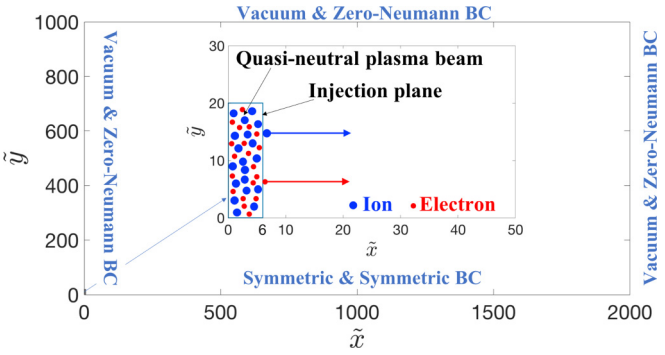

FIG. 1. Schematics of the simulation setup for a collisionless hypersonic beam expansion into a vacuum.

the region of $(\tilde{x}, \tilde{y}) = (0 \sim 6, 0 \sim 20)$. Particles are injected into the simulation domain through the injection plane located at $(\tilde{x}, \tilde{y}) = (6, 0 \sim 20)$. The electric potential of the source is $\tilde{\Phi}_s = 0$, and a zero-electric field condition is used at the simulation domain boundary. Hence, $\tilde{\Phi}_s$ is floating with respect to the ambient. Any particles (mainly the electrons in the fully kinetic PIC simulations) attracted back to the beam source are removed from the simulation domain. At the boundaries of $\tilde{x} = 0$ and 2000, and $\tilde{y} = 1000$, an absorbing boundary condition for particles is also applied. The simulation is considered to be symmetric with respect to $\tilde{y} = 0$, so the specular reflection condition for the particles and the symmetric condition for the Poisson's solver are imposed at $\tilde{y} = 0$. Because of the symmetric boundary with respect to $\tilde{y} = 0$, the beam is considered to have a radius of $R_0 = 20\lambda_{D0}$.

At the plume exit surface, the plume speed is taken to be $\mathbf{v}_0/C_{s0} = (20, 0, 0)$ and the ion temperature is $T_{i0}/T_{e0} = 0.01$. We note that an ion thruster typically operates with the beam Mach number of $M_0 = v_0/C_{s0} = 20 \sim 30$. In the fully kinetic PIC simulations, the real ion-to-electron mass ratios for H^+, Ar^+, and Xe^+ are used. Table I compares some of the mass ratio related parameters at the emission surface used by different simulation runs in this paper. It is noted that m_i/m_e in the present hybrid PIC which uses the Boltzmann electron fluid model can be considered to be ∞.

The simulation domain is discretized with a uniform mesh. The cell size is $\Delta\tilde{x} = \Delta\tilde{y} = 1$. The time step adopted to push the particles is $\Delta\tilde{t} = \Delta t\omega_{pe0} = 0.05$ in all the full PIC simulations, and $\Delta\tilde{t} = \Delta t\omega_{pi0} = 0.01$ in the hybrid PIC simulation, respectively. The simulations are run sufficiently long ($t\omega_{pi0} \geqslant 50$), such that the expansion of plasma plume is well developed, but are terminated when the plasma front is still far away from the outflow boundary to minimize the boundary effects on the expansion. A uniform particle weight is used so the number of macro-particles in a cell scales with the local plasma number density ($\tilde{n}$). Typically, more than 160 million macroparticles are tracked when the simulations are terminated.

TABLE I. Ion-to-electron mass ratio, plasma plume speed, and electron-to-ion plasma frequency ratio at emission surface

Model	m_i/m_e	v_0/C_{s0}	v_0/v_{te0}	$\omega_{pe0}/\omega_{pi0}$
Hybrid PIC	∞	20	—	—
Full PIC (H^+)	1836	20	0.46674	42.85
Full PIC (Ar^+)	72820	20	0.074115	269.85
Full PIC (Xe^+)	241073	20	0.040734	491

III. RESULTS AND DISCUSSIONS

A. Two-dimensional plume expansion

The expansion of a hypersonic plasma plume is an ion timescale process. Here, the simulation results up to $t\omega_{pi} = 50$ are presented. Longer simulations (up to $t\omega_{pi0} = 60$) were run, but not shown, to ensure the conclusions are still valid at later time.

Figure 2 shows the time evolution of the 1D electric potential profiles along the x axis (plume direction) inside the core plume region after the expansion is already well developed. Four distinct plasma regions from the plasma emission source downstream to the vacuum can be observed: (1) the unperturbed plasma region, (2) the quasisteady propagation region, (3) the self-similar expansion region, and (4) the pure electron gas region.

In the unperturbed region (1), the electric potential and plasma density is almost constant. The formation mechanism of the unperturbed region in a high-speed plasma plume was discussed in detail in Ref. [42]. The process is similar to the expansion process of a supersonic neutral gas flow, as pointed out in Refs. [47,48]. The boundary separating the unperturbed region from the plasma expansion region should be the first Mach line originating at the edge of plasma emission source exit $(\tilde{x}, \tilde{y}) = (6, 20)$. This is evident in the 2D plots shown in Figs. 3 and 4. Figure 3 shows the potential isocontours and the electric field vectors, and Fig. 4 shows the isocontour lines of the ion and electron densities. The black dashdot lines overlaid in Figs. 3 and 4 are the first Mach line. The slope of the line k is computed as

$$k = \tan(\theta), \qquad \text{where } \theta \simeq \sin^{-1}\frac{1}{M_0}. \tag{7}$$

It is clear that, within the region bounded by the beam injection plane and the first Mach line, there are negligible variations in the potential and the plasma density. In Fig. 2(c), this unperturbed region is nearly invisible because the two boundaries are too close to each other.

Next to the unperturbed region behind the Mach line is the quasisteady expansion region (2), where the plasma plume structure is similar to that of the Prandtl-Meyer expansion fan in a supersonic gas flow. It can be seen from Fig. 2 that in this region the potential profiles at the earlier time are overlaid with the ones at the later time for all the models. The quasisteady expansion region ends at a deflection point where the potential starts to decrease rapidly. The lines obtained from the full PIC runs for different ion-to-electron mass ratios are almost indistinguishable in Fig. 2. The hybrid PIC model predicts a faster decline in the potential profiles than the full PIC simulations in this region.

The quasisteady expansion region is followed by a region with a linear decrease in potential. It is apparent in Fig. 2 that the slope of the potential profile almost precisely equals $-1/(t\omega_{pi})$. It is notable that the self-similar solution

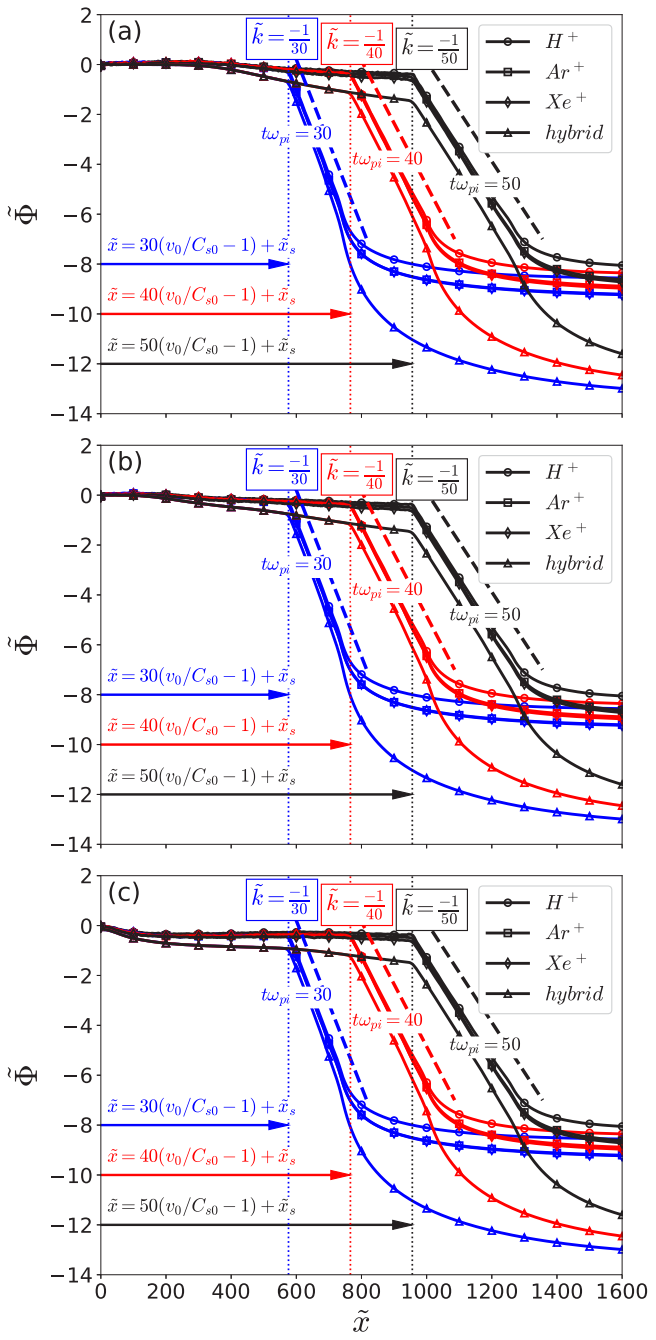

FIG. 2. One-dimensional electric potential profiles along the x axis (plume direction) inside the core region for $t\omega_{pi}=30$ (blue), 40 (red), and 50 (black). The profiles are extracted along $\tilde{y}=$ (a) 0, (b) 10, and (c) 18.

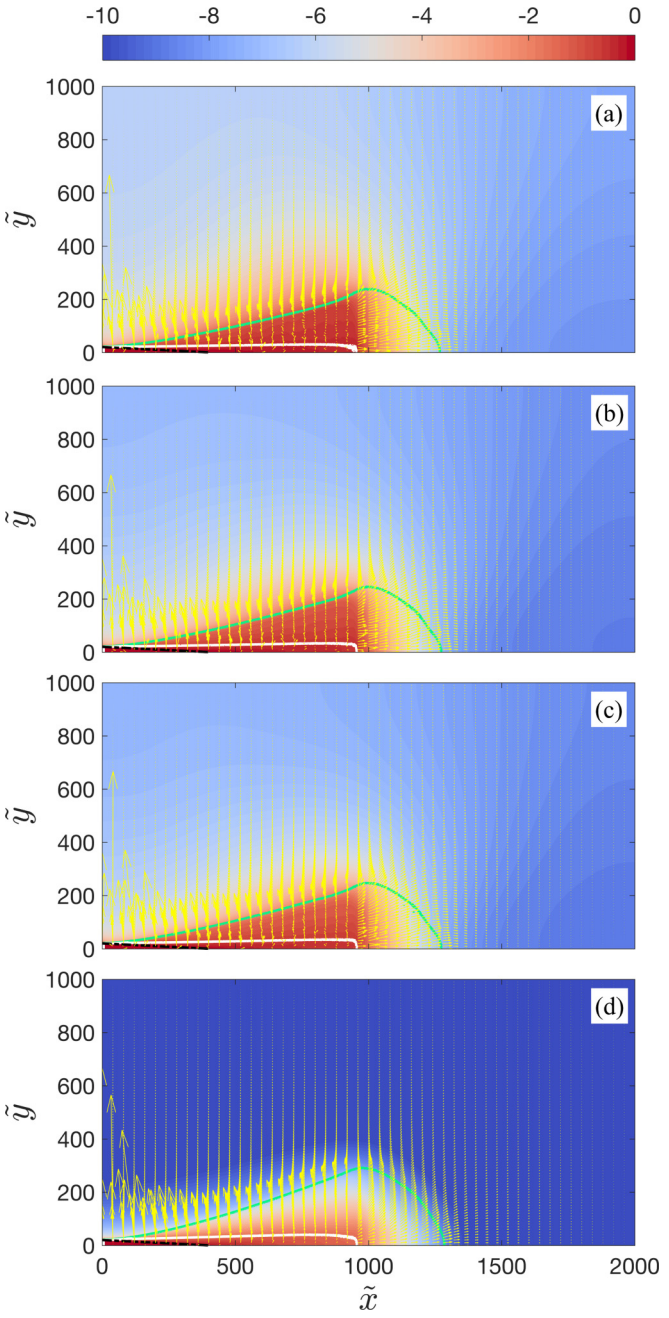

FIG. 3. Isocontours of the electric potential at $t\omega_{pi}=50$ for the full PIC results with (a) H^+, (b) Ar^+, (c) Xe^+, and (d) the hybrid PIC result. Yellow arrows show the electric field vectors. Black dashdot lines ("– . –") are the calculated first Mach lines. The inner white and outer green solid lines correspond to the ion density iso-lines with the values of $\tilde{n}_i(\tilde{x}=50[\tilde{v}_0/C_{s0}-1]+\tilde{x}_s,\tilde{y}=0)$ and $\simeq 0$, respectively.

by Gurevich *et al.* [5] predicts $e\Phi/(k_bT_e)=-1-x/(tC_s)$ or $\tilde{\Phi}=-1-\tilde{x}/(t\omega_{pi})$. Therefore, this linearly decreasing potential region is recognized as the self-similar expansion region (3).

One of the most remarkable features observed is that the deflection point between regions (2) and (3) propagates downstream along the x axis with a constant speed for all the models considered in this study. In Fig. 2, we show, for $t\omega_{pi}=30$, 40, and 50, the vertical dotted lines calculated from

$$\tilde{x}-\tilde{x}_s=t\omega_{pi}(v_0-C_{s0})/C_{s0}=t\omega_{pi}(M_0-1), \quad (8)$$

where $\tilde{x}_s=6$ denotes the position of the source injection plane. It is evident that these vertical dotted lines match the boundaries, as indicated by the deflection points on the potential profiles, between the quasisteady and the self-similar expansion regions.

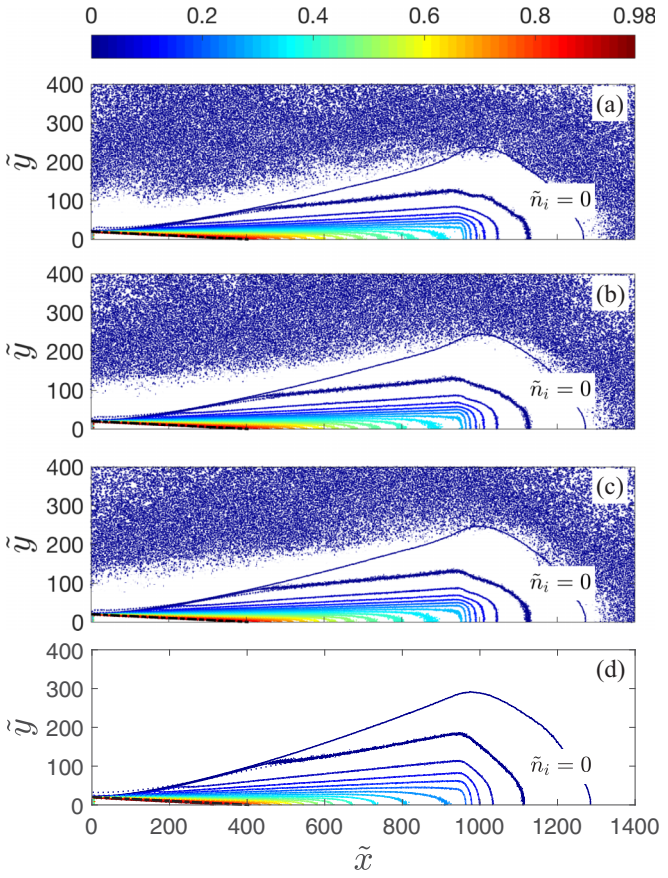

FIG. 4. Iso-contour lines of the ion ("—") and electron ("– – –") number density at $t\omega_{pi} = 50$ for the full PIC results with (a) H^+, (b) Ar^+, (c) Xe^+, and (d) the hybrid PIC result. Black dashdot lines ("– . –") are the calculated first Mach lines.

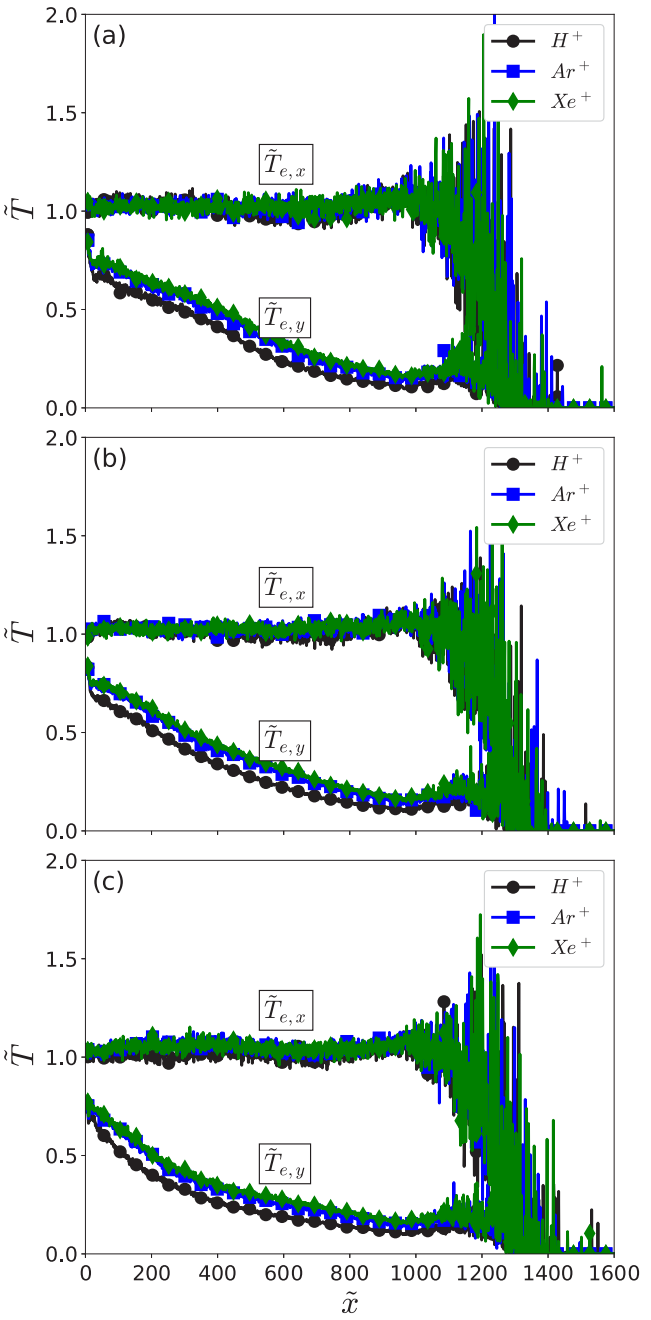

FIG. 5. One-dimensional electron temperature profiles inside the core plume region for $t\omega_{pi} = 50$ extracted along $\tilde{y}$ = (a) 0, (b) 10, and (c) 18.

The self-similar solution to the expansion of a 1D semi-infinite collisionless plasma into a vacuum by Gurevich *et al.* [5] predicts a rarefaction wave propagating inward towards the unperturbed plasma with the ion acoustic velocity. The dynamics of the moving boundary of the quasisteady expansion region is determined by the combination of the plasma plume's downstream propagation and the rarefaction wave's upstream propagation. Consequently, the propagation speed of the boundary (deflection point) should equal $v_0 - C_{s0}$ instead of v_0.

Gurevich's self-similar solution is based on the isothermal electron assumption so the ion acoustic velocity does not change in the process. Accordingly, the observed constant propagation speed along the plume (x) direction implies that the electrons in the quasisteady expansion region must be isothermal in the plume direction. Figure 5 shows the electron temperature profiles at $t\omega_{pi0} = 50$ extracted at the same locations as those in Fig. 2. $\tilde{T}_{e,x}$ and $\tilde{T}_{e,y}$ denote the x and the y component of electron temperature, respectively. The electron temperature exhibits a strong anisotropic feature in the plasma plume. We find that $\tilde{T}_{e,x}$ is almost constant ($\simeq$1) in the entire unperturbed and quasisteady expansion regions while $\tilde{T}_{e,y}$ experiences a considerable decrease as soon as the electrons are emitted from the source. The nearly uniform $\tilde{T}_{e,x}$ is consistent with the observed constant propagation speed along the plume (x) direction of the quasisteady expansion region's boundary. Such a behavior is closely related to the electric field characteristics. The boundary of the quasisteady expansion region, shown by the inner white solid line in Fig. 3, is considered to be the ion density isoline with the value equal to $\tilde{n}_i$ at $(\tilde{x}, \tilde{y}) = (t\omega_{pi}[M_0 - 1] + \tilde{x}_s, 0)$. A careful examination reveals that, except for some random noise inherent in particle simulations, the x component of the electric field, E_x, is nearly negligible. On the other hand, there is a significant positive y-component, E_y, near the boundary of the unperturbed region. E_y decreases with $\tilde{x}$ inside the quasisteady

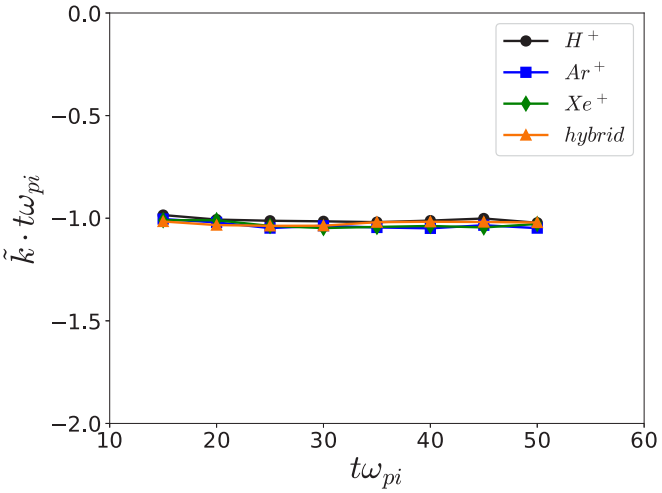

FIG. 6. Fitted value of the normalized slope of the electric potential profile in the self-similar expansion region as a function of time.

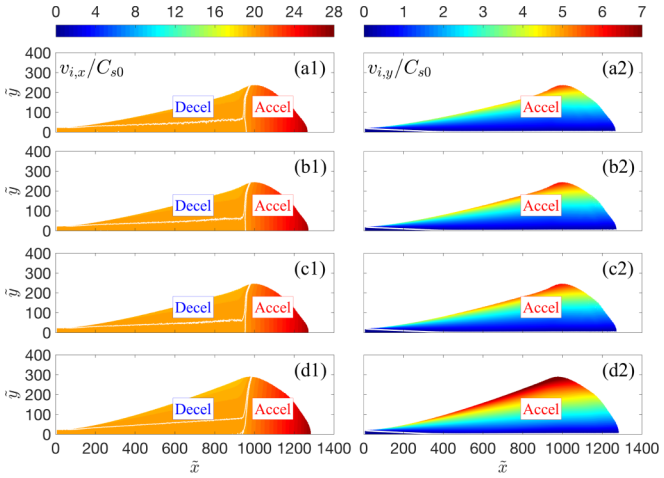

FIG. 7. Ion velocity contours at $t\omega_{pi} = 50$ for the full PIC results with (a) H^+, (b) Ar^+, (c) Xe^+, and (d) the hybrid PIC result. The x-component and the y-component ion velocities normalized by C_{s0} are shown on the left panel (1) and the right panel (2), respectively.

propagation region. As the plasma expands into the vacuum, the electrons experience no force along the plume (x) direction and hence no energy loss. In the transverse (y) direction, the electrons must overcome the electrostatic force, which leads to the temperature decrease in that direction. The transverse electric field component in the quasisteady expansion region is also responsible for the slow decrease in the potential profiles observed in Fig. 2.

Figure 3 clearly shows that E_x jumps from nearly zero in the quasisteady expansion region abruptly to a finite value in the self-similar region immediately downstream of the boundary between the two regions. It also shows that E_y is nearly negligible for $\tilde{y} < 20$ and then slowly increases with $\tilde{y}$ for $\tilde{y} > 20$ in this self-similar expansion region. In response to the electric field, $\tilde{T}_{e,x}$ decreases quickly as the electrons overcome the electrostatic force in the x-direction while $\tilde{T}_{e,y}$ keeps almost constant in the self-similar expansion region, as clearly shown in Fig. 5. The self-similar expansion feature of this region, once established, is preserved over time. This is demonstrated by Fig. 6, which shows the product of $t\omega_{pi}$ and the fitted dimensionless slope $\tilde{k}$ of the potential profile in the self-similar expansion region as a function of $t\omega_{pi}$. We find that the values of $\tilde{k} \cdot t\omega_{pi}$ are approximately -1, with the variation less than 5%, for all the models considered in this study when $t\omega_{pi} \geqslant 15$.

The self-similar expansion region ends near the ion front. It is worth mentioning that the self-similar solution to the 1D semi-infinite collisionless plasma expansion problem fails near the ion front due to effects of charge separation [7]. The 2D ion front is displayed with the green solid line in Fig. 3, and marked with $\tilde{n}_i = 0$ in Fig. 4. The region beyond the ion front contains only electrons of very low density, as shown in Fig. 4. Previous 1D simulations [7,8,10] have shown that the strength of electric field achieves a maximum near the ion front. The present simulations show that, in general, such an observation still holds in the 2D expansion, despite of the much more complex 2D electric field structures. The electrostatic force at the ion front drives the propagation of the ion front.

B. Ion dynamics

In a plasma plume expansion, the overall plume dynamics and plume structure are mainly determined by the ion dynamics. Figure 7 shows the ion velocity contours at $t\omega_{pi} = 50$ for all the models considered in this study. In contrast to the 1D plasma expansion where only ion acceleration is possible, the 2D plasma expansion exhibits a more complex ion velocity field. Figure 7 (left panel) shows that both acceleration and deceleration regions exist for the x component of ion velocity, $v_{i,x}$. The acceleration region ($v_{i,x}/C_{s0} > M_0 + 1\%\Delta\tilde{v}_{i,x}^{\max}$) and deceleration region ($v_{i,x}/C_{s0} < M_0 - 0.2\%\Delta\tilde{v}_{i,x}^{\max}$) are illustrated with the white solid lines as the borders on top of the $v_{i,x}$ contour. Here, $\Delta\tilde{v}_{i,x}^{\max}$ is defined as $v_{i,x}^{\max}/C_{s0} - M_0$, the velocity increase in the x direction of the fastest ions. In the plume core region, the ions are neither accelerated nor decelerated along the x direction. Substantial accelerations for the ions are seen beyond the plume core region. It is interesting to note that the ions are decelerated in region outside of the core region in the transverse direction. The acceleration and deceleration regions are consistent with the electric field shown in Fig. 3. The electric field has a large positive $E_x\hat{x}$ in the acceleration region, and a negative $E_x\hat{x}$ in the deceleration region.

Figure 7 (right panel) shows that the y-component ion velocity ($v_{i,y}$) is accelerated immediately outside the unperturbed region. $v_{i,y}$ experiences no deceleration. The boundary of the acceleration region, shown by the white solid line in Fig. 7 (right panel), is set to be $v_{i,y}/C_{s0} = \%1\Delta\tilde{v}_{i,y}^{\max}$, where $\Delta\tilde{v}_{i,y}^{\max} = v_{i,y}^{\max}/C_{s0}$ is the velocity increase in the y direction of the fastest ions. This line approximately agrees with the boundary of the unperturbed region.

One can see from Fig. 7 that both $v_{i,x}^{\max}$ and $v_{i,y}^{\max}$ in the hybrid simulation result are apparently larger than those in the full PIC results. The difference among the full PIC simulations with various ion masses is almost invisible in the 2D contours. Therefore, a careful examination of the model effects on the ion acceleration process is necessary.

Figure 8 shows the velocity increase of the fastest ions varying with time for $t\omega_{pi} = 5 \sim 50$. In Fig. 8, the symbols

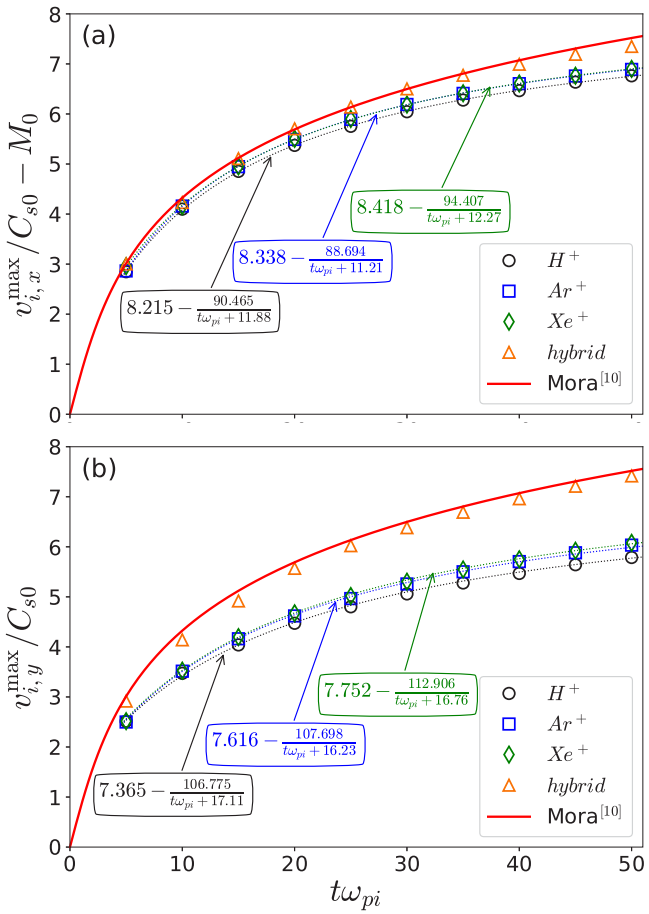

FIG. 8. Velocity increase of fastest ions as a function of time: (a) $v_{i,x}^{max}/C_{s0} - M_0 = \Delta\tilde{v}_{i,x}^{max}$, (b) $v_{i,y}^{max}/C_{s0} = \Delta\tilde{v}_{i,y}^{max}$. The present simulation results from different models are represented by symbols. The red solid line is the prediction of Eq. (9) from Mora's work [10]. The dotted lines are the curves best fitted to the full PIC simulation results with different ion species according to Eq. (10).

denote the simulation results from different models used in this study. For both $v_{i,x}^{max}$ [Fig. 8(a)] and $v_{i,y}^{max}$ [Fig. 8(b)], the hybrid model predicts higher velocity increases than all the three full PIC models. The values of $\Delta\tilde{v}_{i,x}^{max}$ and $\Delta\tilde{v}_{i,y}^{max}$ are similar to each other for all the time in the hybrid PIC simulation. However, the full PIC simulations predict a considerably larger ion velocity increase in the x direction than that in the y direction. Furthermore, different ion masses also affect the ion accelerations in the full PIC simulations. A higher ion mass yields a larger amount of acceleration in both $v_{i,x}^{max}$ and $v_{i,y}^{max}$.

Also presented by the red solid line in Fig. 8 is the time dependence of ion front velocity from Mora's semi-analytical formula [10],

$$v_i/C_{s0} = 2\ln(\tau + \sqrt{\tau^2+1}), \tag{9}$$

where $\tau = t\omega_{pi}/\sqrt{2e_N}$ and the constant $e_N = 2.718\,28\ldots$ is the Euler's number. We find that the prediction of Eq. (9) agrees well with the present hybrid PIC results, even though Eq. (9) is derived from the expansion of a 1D semi-infinite plasma while the present simulation is for a 2D finite-size plume. Nevertheless, such an agreement is not surprising since

TABLE II. Best fitted parameters to ion velocity increase in the x direction [Eq. (10a)].

Model (ion species)	p_0	p_1	p_2	RMSE$(\Delta\tilde{v}_{i,x}^{max})$
H^+	8.215	90.465	11.88	0.95%
Ar^+	8.338	88.694	11.21	0.42%
Xe^+	8.418	94.407	12.27	0.97%

the derivation of Eq. (9) is based on the same assumption that the electrons can be considered as a massless, isothermal fluid and described by the Boltzmann relation Eq. (1). This assumption gives the electrons an infinite amount of energy to drive the plasma expansion. Therefore, the hybrid model tends to overestimate the ion acceleration, as shown in Fig. 8.

When the electron kinetics is fully taken into account, no analytical expression for the dependence of the ion acceleration is available in the literature. We fit the present full PIC data of ion velocity increases in the x and y directions to the expression given as follows,

$$v_{i,x}^{max}(t)/C_{s0} - M_0 = \Delta\tilde{v}_{i,x}^{max} = p_0 - \frac{p_1}{t\omega_{pi} + p_2}, \tag{10a}$$

$$v_{i,y}^{max}(t)/C_{s0} = \Delta\tilde{v}_{i,y}^{max} = q_0 - \frac{q_1}{t\omega_{pi} + q_2}, \tag{10b}$$

where $p_{0,1,2}$ and $q_{0,1,2}$ are the fitted parameters to be determined. The best fitted parameters to Eqs. (10a) and (10b) are listed in Tables II and III, respectively. RMSE in the tables denotes the root mean square error defined as

$$\mathrm{RMSE}(f) = \sqrt{\frac{\sum_{t=1}^{n}(\hat{f}_t - f_t)^2}{n}}. \tag{11}$$

where f represents either $\Delta\tilde{v}_{i,x}^{max}$ or $\Delta\tilde{v}_{i,y}^{max}$, and $\hat{f}_t$ denotes the predicted value by the fitting formula with respect to the tth data point f_t from the simulation results. The error of the fitting expression given in Eq. (10) is less than 1% and 3% for the acceleration of the fastest ions in the plume and transverse directions, respectively. The best fitted curves of $\Delta\tilde{v}_{i,x}^{max}$ and $\Delta\tilde{v}_{i,y}^{max}$ are also presented in Fig. 8 by the dotted lines.

The final velocity gains of the fastest ions can be extrapolated from Eq. (10), that is, $v_{i,x}^{max}(t\to\infty)/C_{s0} - M_0 = p_0$ and $v_{i,y}^{max}(t\to\infty) = q_0$. Figure 9 shows the ion mass dependence of the final velocity gain of the fastest ions. It is found that both $\Delta\tilde{v}_{i,x}^{max}$ and $\Delta\tilde{v}_{i,y}^{max}$ scale with $\sqrt{m_i/m_e}$, but $\Delta\tilde{v}_{i,y}^{max}$ shows a stronger dependence on $\sqrt{m_i/m_e}$. Denavit [8] showed that the electron cooling was inversely proportional to $\sqrt{m_i/m_e}$. Therefore, a larger value of m_i/m_e corresponds to less effective electron cooling, and thus a higher electron temperature. This

TABLE III. Best fitted parameters to ion velocity increase in the y direction [Eq. (10b)].

Model (ion species)	q_0	q_1	q_2	RMSE$(\Delta\tilde{v}_{i,y}^{max})$
H^+	7.365	106.775	17.11	2.73%
Ar^+	7.616	107.698	16.23	2.73%
Xe^+	7.752	112.906	16.76	2.34%

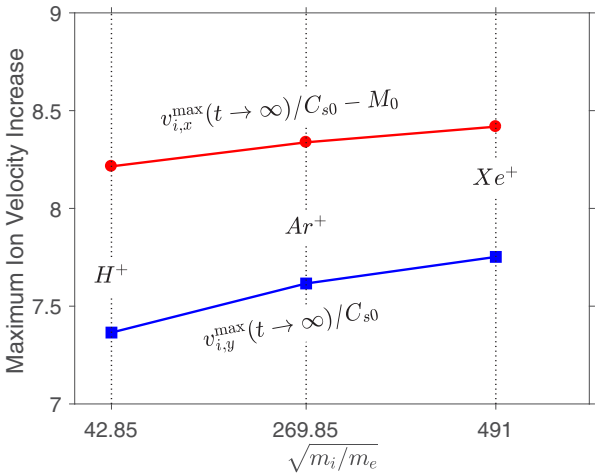

FIG. 9. Dependence of final velocity increase of the fastest ions on mass ratio.

can be clearly seen from the $\tilde{T}_{e,y}$ profiles in Fig. 5. The energy to drive the ion front motion comes from the electron thermal energy. A plume with heavier ions tends to preserve a higher electron temperature. This allows the ions to be accelerated to a higher final velocity. Finally, the observation that $\Delta\tilde{v}_{i,x}^{\max}$ shows less dependence on the ion mass than $\Delta\tilde{v}_{i,y}^{\max}$ can be attributed to the fact that the electron cooling is more effective in the y-direction. The reason is that, as shown in Fig. 5, $\tilde{T}_{e,x}$ is almost constant until the self-similar expansion region while $\tilde{T}_{e,y}$ decreases throughout most of the plume region.

C. Effects of electron characteristics

A comparison of the full PIC and hybrid PIC simulation results in the previous sections shows that, in addition to the quantitative difference in plume potential and density, the hybrid PIC using the Boltzmann electron fluid model does not resolve the difference in plume expansion in the plume direction versus that in the transverse direction as shown in the full PIC results. This qualitative difference is attributed to the strong anisotropy in the electron temperature that is omitted by the hybrid PIC modeling.

Past studies have shown that the 1D plasma expansion may be classified as the semi-infinite plasma expansion or the finite plasma expansion. For a freely expanding plasma in 1D, there exists a rarefaction wave propagating inward towards the plasma with the ion acoustic speed of C_s. Therefore, for a timescale t, a semi-infinite plasma refers to a plasma with a size $L > C_s t$ such that the rarefaction wave front cannot reach the plasma center and an unperturbed plasma region always exists, while a finite plasma has a size $L < C_s t$ and thus the entire plasma is affected by the expansion. Hence, for the 2D hypersonic plasma plume considered in this study, the expansion along the plume direction can be considered similar to a 1D semi-infinite plasma expansion, while that along the transverse expansion is similar to a 1D finite plasma expansion.

The main difference between the semi-infinite plasma and finite plasma expansion is the completely different electron thermodynamics involved. The semi-infinite plasma serves as a reservoir with an unlimited amount of energy such that the change of electron temperature may be ignored. Consequently, the isothermal electron fluid model is a good approximation for the expansion of a semi-infinite plasma into a vacuum. The effect of electron cooling was found to be proportional to $(m_i/m_e)^{-1/2}$ [8,9]. In particular, Denavit [8] fitted the kinetic simulation results to the polytropic relation Eq. (12) to study the cooling effects of electrons in a semi-infinite plasma expansion,

$$\frac{T_e}{n_e^{\gamma-1}} = \text{const}, \quad \text{or} \quad \frac{p_e}{n_e^{\gamma}} = \text{const}, \tag{12}$$

where γ is the polytropic coefficient. $\gamma = 1$ corresponds to the isothermal process, and $\gamma = 3, 2,$ or $5/3$ indicates the adiabatic process in 1D, 2D, or 3D, respectively. Denavit's [8] fitting showed $\delta\gamma = \gamma - 1$ is as small as 0.011 when $m_i/m_e = 1600$. This suggests that the use of the isothermal electron model in the semi-infinite plasma expansion problems may be justified because electron cooling is negligible. However, for a finite plasma expansion, assuming the electrons are isothermal is inappropriate because only a finite amount of electron energy is available to drive the expansion. It was noted that the electron temperature can decrease as fast as proportional to t^{-2} in a finite plasma if no external energy is supplied [13,15,16]. Consequently, the electron cooling plays an important role in the expansion of a finite plasma.

The polytropic relation Eq. (12) with an isotropic electron temperature and a fixed value of γ was incorporated into hybrid PIC codes to study the thruster plume expansion [31]. While this approach is more general than the isothermal electron approximation, the issue whether the electrons in a collisionless hypersonic plasma plume may be approximated by a simple thermodynamic relation remains. Figure 10 shows $\tilde{n}_e$-$\tilde{T}_e$ relation in a log-log scale by extracting the flow field data at the same locations in Fig. 5. According to Eq. (12), the slope of a line in the $\log_{10}(\tilde{n}_e)$-$\log_{10}(\tilde{T}_e)$ plot is $\delta\gamma$. Clearly, the expansion in the plume (x) direction is almost isothermal. The electron cooling in the transverse (y) direction depends on not only the ion mass but also the positions in the plume. The cooling is apparently not a typical adiabatic process. Hence, using a simple polytropic relation with a constant γ and an isotropic T_e is insufficient to model the complex electron dynamics for the collisionless hypersonic plasma plume.

The near constant $\tilde{T}_{e,x}$ and the decrease of $\tilde{T}_{e,y}$ shown in Fig. 10 support the aforementioned analogy of the 2D collsionless hypersonic plasma plume expansion to the two well studied 1D expansion models. The distinct ion acceleration processes along the plume and transverse directions, e.g., smaller $\Delta\tilde{v}_{i,y}^{\max}$ than $\Delta\tilde{v}_{i,x}^{\max}$, seen in the full PIC simulations are due to such anisotropic characteristics of the electron temperature. These observations suggest that to accurately describe the electron dynamics in a collisionless plasma plume expansion with a fluid model, one needs to take into account the strong anisotropy in electron characteristics and solve for the equivalent electron temperature in the plume direction and the transverse direction separately.

IV. CONCLUSIONS

The expansion of a collisionless, hypersonic plasma plume into a vacuum is simulated using both the hybrid and fully

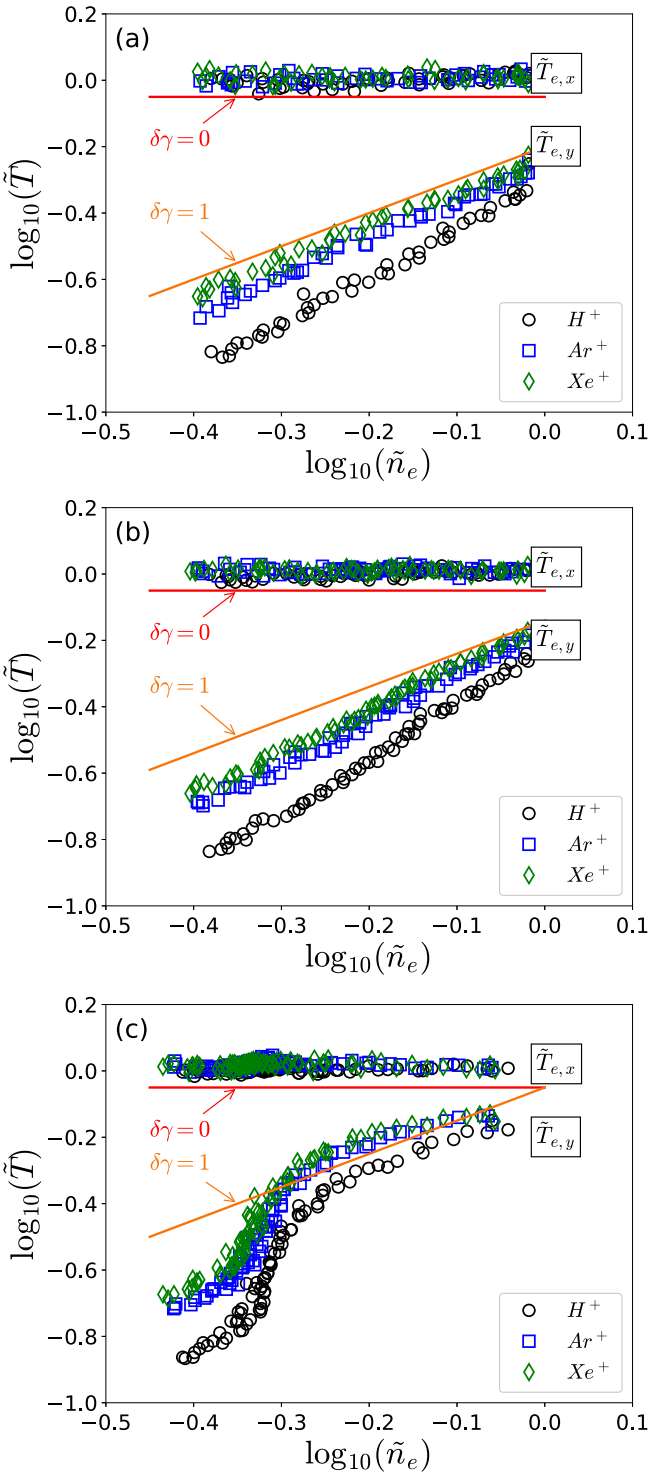

FIG. 10. Relation of $\tilde{T}_e$ to $\tilde{n}_e$ inside the steady core plume region for $t\omega_{pi} = 50$ extracted along $\tilde{y} =$ (a) 0, (b) 10, and (c) 18.

kinetic PIC models. The hybrid PIC model considers the electrons as a massless isothermal fluid. The full PIC simulations are carried out using the real ion-to-electron mass ratios for H^+, Ar^+, and Xe^+. Both the hybrid and full PIC simulations reveal that the plume structure exhibits four distinct expansion regions. These regions are identified as, from the plasma emission plane to the downtream along the plume direction, the unperturbed, quasisteady expansion, self-similar expansion and electron front regions, respectively. The formation of the unperturbed region, bounded by the Mach cone, is similar to the process of a supersonic neutral gas expansion. The establishment of the quasisteady propagation region is due to the combined effect of the forward plume propagation and the backward rarefaction wave propagation. The self-similar expansion mechanism in the hypersonic plasma plume is recognized the same as that in the 1D semi-infinite plasma expansion.

The electron temperatures are shown to be highly anisotropic in the plume. $T_{e,x}$ is almost unchanged from the source until the self-similar region, while $T_{e,y}$ drops drastically immediately downstream of the injection plane. A consequence of the anisotropic electron temperatures is the different accelerations that the fastest ions can achieve. A higher electron temperature generally results in a larger ion acceleration. Besides, a smaller ion mass leads to a more rapid electron temperature decrease and thus a lower electron temperature in the transverse direction. The saturated accelerations of the fastest ions are obtained by extrapolating the present data to the time at infinity. The extrapolated saturated ion accelerations scale with $\sqrt{m_i/m_e}$.

The anisotropic electron thermodynamics leads to very different expansion features along the plume emission direction and the transverse direction. The results show that the expansion along the plume direction is similar to that described by the 1D semi-infinite plasma model and that the electrons are mostly isothermal in that direction. However, the expansion transverse to the plume is analogous to a 1D finite plasma expansion situation, where the thermal energy is limited and thereby the electron cooling effect on the expansion is important.

The fully kinetic PIC is used to benchmark the commonly used hybrid PIC simulation of plume simulation. The comparison between the hybrid and full PIC results shows that modeling electrons either as an isothermal fluid or as a polytropic fluid with an isotropic temperature is oversimplified and leads to not only quantitative but also qualitative differences. In order for an electron fluid approximation to be applicable, the model must at least have the capability of resolving the strong anisotropic thermodynamics for electrons.

ACKNOWLEDGMENTS

The simulations in this paper were performed at the Center for High-Performance Computing of the University of Southern California.

[1] J. Wang, D. E. Brinza, D. T. Young, J. E. Nordholt, J. E. Polk, M. D. Henry, R. Goldstein, J. J. Hanley, D. J. Lawrence, and M. Shappirio, J. Spacecr. Rockets **37**, 545 (2000).

[2] J. Wang, D. Brinza, and M. Young, J. Spacecr. Rockets **38**, 433 (2001).
[3] J. Wang, O. Chang, and Y. Cao, IEEE Trans. Plasma Sci. **40**, 230 (2012).
[4] J. Wang, D. Han, and Y. Hu, IEEE Trans. Plasma Sci. **43**, 3047 (2015).
[5] A. V. Gurevich, L. V. Pariiskaya, and L. P. Pitaevskii, Sov. Phys. JETP **22**, 449 (1966) [J. Exptl. Theoret. Phys. (U.S.S.R.) **49**, 647 (1965)].
[6] J. E. Allen and J. G. Andrews, J. Plasma Phys. **4**, 187 (1970).
[7] J. E. Crow, P. L. Auer, and J. E. Allen, J. Plasma Phys. **14**, 65 (1975).
[8] J. Denavit, Phys. Fluids **22**, 1384 (1979).
[9] P. Mora and R. Pellat, Phys. Fluids **22**, 2300 (1979).
[10] P. Mora, Phys. Rev. Lett. **90**, 185002 (2003).
[11] Y. Huang, Y. Bi, X. Duan, X. Lan, N. Wang, X. Tang, and Y. He, Appl. Phys. Lett. **92**, 031501 (2008).
[12] J. E. Allen and M. Perego, Phys. Plasmas **21**, 034504 (2014).
[13] G. Manfredi, S. Mola, and M. Feix, Phys. Fluids B **5**, 388 (1993).
[14] A. V. Baitin and K. M. Kuzanyan, J. Plasma Phys. **59**, 83 (1998).
[15] D. S. Dorozhkina and V. E. Semenov, Phys. Rev. Lett. **81**, 2691 (1998).
[16] P. Mora, Phys. Rev. E **72**, 056401 (2005).
[17] P. Mora, Phys. Plasmas **12**, 112102 (2005).
[18] M. Murakami and M. M. Basko, Phys. Plasmas **13**, 012105 (2006).
[19] T. Grismayer and P. Mora, Phys. Plasmas **13**, 032103 (2006).
[20] T. Grismayer, P. Mora, J. C. Adam, and A. Héron, Phys. Rev. E **77**, 066407 (2008).
[21] P. Mora and T. Grismayer, Phys. Rev. Lett. **102**, 145001 (2009).
[22] C. K. Birdsall and A. B. Langdon, *Plasma Physics via Computer Simulation* (CRC Press, Boca Raton, FL, 2004).
[23] R. I. S. Roy and D. E. Hastings, J. Spacecr. Rockets **33**, 519 (1996).
[24] D. Y. Oh, D. E. Hastings, C. M. Marrese, J. M. Haas, and A. D. Gallimore, J. Propul. Power **15**, 345 (1999).
[25] J. Wang, Y. Cao, R. Kafafy, J. Pierru, and V. K. Decyk, IEEE Trans. Plasma Sci. **34**, 2148 (2006).
[26] B. Korkut and D. A. Levin, J. Propul. Power **33**, 264 (2017).
[27] R. I. S. Roy, D. E. Hastings, and N. A. Gatsonis, J. Spacecr. Rockets **33**, 525 (1996).
[28] D. B. VanGilder, I. D. Boyd, and M. Keidar, J. Spacecr. Rockets **37**, 129 (2000).
[29] I. D. Boyd and J. T. Yim, J. Appl. Phys. **95**, 4575 (2004).
[30] F. Taccogna, D. Pagano, F. Scortecci, and A. Garulli, Plasma Sources Sci. Technol. **23**, 065034 (2014).
[31] F. Cichocki, A. Domínguez-Vázquez, M. Merino, and E. Ahedo, Plasma Sources Sci. Technol. **26**, 125008 (2017).
[32] B. N. Breizman and A. V. Arefiev, Phys. Plasmas **14**, 073105 (2007).
[33] A. V. Arefiev and B. N. Breizman, Phys. Plasmas **15**, 042109 (2008).
[34] A. V. Arefiev and B. N. Breizman, Phys. Plasmas **16**, 055707 (2009).
[35] M. Martinez-Sanchez, J. Navarro-Cavallé, and E. Ahedo, Phys. Plasmas **22**, 053501 (2015).
[36] M. Merino, J. Mauriño, and E. Ahedo, Plasma Sources Sci. Technol. **27**, 035013 (2018).
[37] C. Othmer, K. Glassmeier, U. Motschmann, J. Schüle, and C. Frick, Phys. Plasmas **7**, 5242 (2000).
[38] A. Wheelock, D. Cooke, and N. A. Gatsonis, Comput. Phys. Commun. **164**, 336 (2004).
[39] L. Brieda and J. Wang, in *Proceedings of the 41st AIAA/ASME/SAE/ASEE Joint Propulsion Conference & Exhibit, TUCSON, AZ* (AIAA, Reston, VA, 2005), paper AIAA 2005-4045.
[40] H. Usui, A. Hashimoto, and Y. Miyake, J. Phys.: Conf. Ser. **454**, 012017 (2013).
[41] Y. Hu and J. Wang, IEEE Trans. Plasma Sci. **43**, 2832 (2015).
[42] Y. Hu and J. Wang, Phys. Plasmas **24**, 033510 (2017).
[43] J. Psikal, V. Tikhonchuk, J. Limpouch, A. Andreev, and A. Brantov, Phys. Plasmas **15**, 053102 (2008).
[44] T. Arber, K. Bennett, C. Brady, A. Lawrence-Douglas, M. Ramsay, N. Sircombe, P. Gillies, R. Evans, H. Schmitz, A. Bell *et al.*, Plasma Phys. Control. Fusion **57**, 113001 (2015).
[45] A. Arefiev, T. Toncian, and G. Fiksel, New J. Phys. **18**, 105011 (2016).
[46] M. Pfeiffer, S. Copplestone, T. Binder, S. Fasoulas, and C.-D. Munz, *30th International Symposium on Rarefied Gas Dynamics*, AIP Conf. Proc. 1786 (AIP, Melville, NY, 2016), p. 130005.
[47] J. Wang and D. E. Hastings, Phys. Fluids B **4**, 1597 (1992).
[48] J. Wang and D. E. Hastings, Phys. Fluids B **4**, 1615 (1992).